International Journal of Heat and Mass Transfer 52 (2009) 5719–5730

Contents lists available at ScienceDirect

International Journal of Heat and Mass Transfer

journal homepage: www.elsevier.com/locate/ijhmt

Effect of heat and mass transfer on non-Newtonian flow – Links to atherosclerosis

Sarifuddin, Santabrata Chakravarty, Prashanta Kumar Mandal *

Department of Mathematics, Visva-Bharati University, Santiniketan, 731235 WB, India

ARTICLE INFO

Article history:
Received 10 July 2008
Received in revised form 22 December 2008
Accepted 16 April 2009
Available online 28 September 2009

Keywords:
Generalized Newtonian
Heat and mass transfer
Irregular stenosis
Sherwood number
MAC method

ABSTRACT

The present investigation deals with a mathematical model representing the dynamic response of heat and mass transfer to blood streaming through the arteries under stenotic condition. The blood is treated to be a generalized Newtonian fluid and the arterial wall is considered to be rigid having differently shaped stenoses in its lumen arising from various types of abnormal growth or plaque formation. The nonlinear unsteady pulsatile flow phenomenon unaffected by the concentration-field of the macromolecules is governed by the Navier–Stokes equations together with the equation of continuity while those of the heat and the mass transfers are controlled by the heat conduction and the convection–diffusion equations, respectively. The governing equations of motion accompanied by the appropriate choice of the boundary conditions are solved numerically by Marker and Cell (MAC) method in order to compute the physiologically significant quantities with desired degree of accuracy. The necessary checking for numerical stability has been incorporated in the algorithm for better precision of the results computed. The quantitative analysis carried out finally includes the respective profiles of the flow-field, the temperature and the mass concentration along with their individual distributions over the entire arterial segment as well. The key factors like the wall shear stress and the Sherwood number are also examined for further qualitative insight into the heat flow and mass transport phenomena through arterial stenosis. The present results show quite consistency with several existing results in the literature which substantiate sufficiently to validate the applicability of the model under consideration.

1. Introduction

It is an well established fact that atherosclerosis, a kind of arterial disease leading to the malfunction of the cardiovascular system, involves a distinctive accumulation of low-density lipoprotein and other lipid bearing materials in large and medium-size arteries [1]. Such abnormal accumulation implies that the transport of low-density lipoproteins from blood into the arterial walls must play key role in the development of atherosclerotic lesions, which are usually detected at specific locations in the arterial system, particularly near the bends, bifurcations and some other regions identified by complicated flow patterns of the streaming blood [2]. Hemodynamics has long been suspected of being involved atherosclerotic lesions causing the normal flow disturbances around those specific sites where plaques are frequently formed. Beside this, in order to alleviate the heat sink effect of large vessels, considerable attention has also been focused on reducing blood flow by either pharmacologic agent [3] or by occluding arterial inflow [4] as a measure of ablative therapies for treatment of abnormal and undesirable growth in vascular lumen. It is well known that large blood vessels perturb the induced temperature distributions in physiological situations. The understandings of the magnitude of the perturbation of the temperature distribution as a function of the vessel diameter and temperature gradient are critical to the development of appropriate models of bioheat transport.

Although it has been found that low and oscillatory wall shear stresses are often positively correlated to localised intimal thickening of the arterial wall [5,6], but the relationship between wall shear stress and atherosclerotic development is yet to be understood as characterized in [7]. There are views that the correlation between wall shear stress and atherosclerosis in some arteries [8,9] can not always be convincingly established, which suggest that wall shear stress may not be the only responsible mechanism that promotes the formation of atherosclerotic lesions. Caro et al. [10,11] postulated that atherosclerosis may occur due to shear-dependent mass transfer mechanism of cholesterol between blood and the arterial wall. For the purpose of the appropriate assessment regarding the possible correlation between the sites of atherosclerotic lesions and the patterns of mass transport, accurate characterization of the behaviour of local mass transport is highly necessary. Moreover, good understanding of mass transport in arterial stenoses is of considerable clinical interest in the study of the formation and development of atherosclerotic lesions. The

---

* Corresponding author.
E-mail addresses: santabrata2004@yahoo.co.in (S. Chakravarty), pkmind02@yahoo.co.uk (P.K. Mandal).

0017-9310/$ - see front matter © 2009 Elsevier Ltd. All rights reserved.
doi:10.1016/j.ijheatmasstransfer.2009.04.040

Nomenclature

C	dimensionless mass concentration of fluid
C_p	specific heat [J Kg^{-1} K^{-1}]
C_s	reference concentration at the inlet [n mol/mn^3]
D	diffusivity [mm^2/s]
k'	thermal conductivity [J s^{-1} mm^{-1} K^{-1}]
L	dimensionless length of the arterial segment
p	dimensionless fluid pressure
p'	fluid pressure [N/mm^2]
Pr	Prandtl number $\left[\frac{\mu C_p}{k'}\right]$
r	dimensionless radial coordinate
r_0	dimensional radius of the artery [mm]
Re	Reynolds' number $\left[\frac{\rho U_0 r_0}{\eta_\infty}\right]$
Sc	Schmidt number $\left[\frac{\mu}{\rho D}\right]$
t	dimensionless time
T	dimensionless temperature
T_i	temperature at the inlet [K]
T_w	wall temperature [K]
u	dimensionless radial velocity
U_0	cross-sectional average velocity [mm/s]
w	dimensionless axial velocity
z	dimensionless axial coordinate
z_0	half-length of the stenosis [mm]
z_1	length of the stenosis centre [mm]

Greek symbols

ρ	density [g/mm^3]
η_0	apparent viscosity corresponding to zero shear rate [g/mm s]
η_∞	apparent viscosity corresponding to large shear rate [g/mm s]
λ	dimensionless viscosity
$\wedge$	time dependent material constant [s]
$\dot{\gamma}$	shear rate [s^{-1}]
δ	maximum width of the stenosis [mm]
α	Womersley number $\left[r_0\sqrt{\frac{\omega\rho}{\mu}}\right]$
ω	radial frequency [rad/s]
β	upwinding parameter

presence of stenoses causes flow separation together with complex hemodynamic features and these, in turn, influence mass transport. Back et al. [12] considered a real specimen having a 2D representation of an actual coronary artery as the basis for a computational model of mass transport and computed oxygen fluxes to the arterial wall for unsteady flow conditions. They have shown their interest on the variations of the mass transfer only in the stenotic regions of the specimen contained several stenoses. Their findings indicated a strong reduction in oxygen transport on the rear end of plaques at incipient flow separation zones. Another numerical separation of mass transport was carried out by Ma et al. [13] where the influence of separated flow on luminal mass transport and the arterial mass transfer coefficient was recorded. Subsequently, Rappitsch and Perktold [14] studied numerically the steady convective diffusion processes in an axisymmetric tube having a local constriction by applying a passive transport law for the flux at the wall and physiologically realistic values for the flow and mass transfer parameters.

In the past, there have been quite a good number of studies to examine heat transfer in blood vessels. Charm et al. [15] experimentally investigated heat transfer in small tubes of diameter 0.6 mm in a water bath while Victor and Shah [16,17] computed heat transfer in both the cases for uniform heat flux and uniform wall temperature for fully developed flow and in the entrance region. The correlation equations for estimating the heat transfer under different configurations and diameters of blood vessels were developed by Chato [18]. Based upon the study of laminar and fully thermally developed flow in large vessels, Lagendijk [19] analysed temperature distributions in the entrance region around the vessels during hyperthermia. Barozzi and Dumas [20] calculated heat transfer in the entrance region considering the rheological properties of the blood stream and a cell-free peripheral plasma layer at the vessel wall. The use of the consideration of energy equations was made by Kolios et al. [21] to compute temperature profiles around large vessels since heat transfer coefficients vary during temperature variations. Based on the assumptions of constant vessel wall temperature, Tungjitkusolmn et al. [22] simulated the influence of a large vessel on thermal lesion formation during radio frequency ablation. Their model was subsequently updated by Haemmerich et al. [23] who used the estimates of the heat transfer coefficient to simulate the influence of a large vessel on the formation of thermal lesion during radio frequency ablation by assuming fully thermally developed flow. All these studies were concentrated only on the heat transfer to blood streaming through the arteries but disregarded mass transport processes. One possible reason could have been that the problems dealing with mass transport phenomena are highly convection dominated because of the low diffusion coefficients of the principal constituents governing transportation of blood.

However, to the authors' knowledge there have been some studies [24–27] concerning both heat and mass transfer in non-Newtonian fluids where in the most cases the governing flow was considered to be steady and the effect of non-Newtonian parameters on the flow-field together with the temperature-field were mostly recorded. It is commonly believed that the influence of non-Newtonian property of blood is meagre in larger arteries where the shear rate is high. The above mentioned studies were not, however, performed in stenosed arteries although the atherosclerotic flow phenomenon is of great clinical interest both with respect to genesis and the diagnostics of atherosclerosis.

The objective of the present paper is to study the response of heat and mass transfer of blood flowing through three different types of constrictions in the unsteady state. The arterial wall is considered to be rigid having differently shaped constrictions in its lumen arising from the formation of various types of abnormal growth or plaque and the streaming blood is treated to be generalized Newtonian. The assumption of wall rigidity may not seriously affect the flow since the development of atherosclerosis in arteries causes a significant reduction in the distensibility of its wall as evident from the observation of Nerem [28]. The unsteady nonlinear Navier–Stokes equations of motion governing blood flow, the heat flow and the mass transport equations coupled to the velocity-field are taken up along with the appropriate boundary conditions including inlet–outlet conditions in order to define the present biomechanical problem. Following the radial coordinate transformation, all the governing equations, duly non-dimensionalized, are reduced to a tractable form initially and then they are solved numerically by MAC method using non-uniform grid for their finite-difference representations. An extensive quantitative analysis with substantial accuracy has been performed at the end of the paper in order to exhibit the patterns of the flow-field, the mass concentration profile and the temperature profile over the entire arterial segment. For a more quantitative insight into flow and mass transport patterns in three different types of stenoses, the characteristics of the normalised wall shear stress and the Sherwood number were examined in detail and the effects of severity of the stenoses on them were quantified so as to validate the applicability of the present model with reference to the latest findings in the existing literatures.

2. Mathematical formulation

The streaming blood in the arterial lumen is treated as a generalized Newtonian fluid. The Navier–Stokes' equations and the equation of continuity that govern the unsteady nonlinear fully developed swirl-free flow of blood may be written in dimensionless form as

$$\frac{\partial w}{\partial t}+\frac{\partial(wu)}{\partial r}+\frac{\partial w^2}{\partial z}+\frac{(wu)}{r}=-\frac{\partial p}{\partial z}+\frac{\mu(\dot{\gamma})}{Re}\left[\frac{\partial^2 w}{\partial r^2}+\frac{1}{r}\frac{\partial w}{\partial r}+\frac{\partial^2 w}{\partial z^2}\right]+\frac{1}{Re}\left[\frac{\partial\mu}{\partial r}\left(\frac{\partial u}{\partial z}+\frac{\partial w}{\partial r}\right)+2\frac{\partial\mu}{\partial z}\frac{\partial w}{\partial z}\right], \tag{1}$$

$$\frac{\partial u}{\partial t}+\frac{\partial u^2}{\partial r}+\frac{\partial(wu)}{\partial z}+\frac{u^2}{r}=-\frac{\partial p}{\partial r}+\frac{\mu(\dot{\gamma})}{Re}\left[\frac{\partial^2 u}{\partial r^2}+\frac{1}{r}\frac{\partial u}{\partial r}+\frac{\partial^2 u}{\partial z^2}-\frac{u}{r^2}\right]+\frac{1}{Re}\left[2\frac{\partial\mu}{\partial r}\frac{\partial u}{\partial r}+\frac{\partial\mu}{\partial z}\left(\frac{\partial u}{\partial z}+\frac{\partial w}{\partial r}\right)\right] \tag{2}$$

$$\text{and}\quad r\frac{\partial w}{\partial z}+\frac{\partial(ur)}{\partial r}=0, \tag{3}$$

where r and z are the dimensionless co-ordinates, scaled with respect to r_0, with the z-axis located along the symmetry axis of the artery. As there is no secondary or rotational flow so the total velocity is defined by the dimensionless radial and axial components, u and w scaled with respect to the cross-sectional average velocity U_0. The Reynolds number Re, the dimensionless pressure and the shear-dependent viscosity may be defined as

$$Re=\frac{\rho U_0 r_0}{\eta_\infty},\quad p=\frac{p'}{\rho U_0^2},$$

$$mu(\dot{\gamma})=1+(\lambda-1)\left[\frac{1+log_e(1+\wedge\dot{\gamma})}{1+\wedge\dot{\gamma}}\right]\ \text{(cf. Yeleswarapu [29])} \tag{4}$$

$$\text{with } \dot{\gamma}=\left[2\left(\frac{\partial u}{\partial r}\right)^2+2\left(\frac{\partial w}{\partial z}\right)^2+2\left(\frac{u}{r}\right)^2+\left(\frac{\partial u}{\partial z}+\frac{\partial w}{\partial r}\right)^2\right]^{\frac{1}{2}}, \tag{5}$$

in which ρ is the density of blood, p' the pressure and the non-dimensional viscosity parameters $\lambda=\frac{\eta_0}{\eta_\infty}, \wedge\rightarrow\frac{\wedge U_0}{r_0}$ with η_0 and $\eta_\infty(\eta_0\geqslant\eta_\infty)$ are the asymptotic apparent viscosities as $\dot{\gamma}\rightarrow 0$ and ∞, respectively, and $\wedge\geqslant 0$ is a material constant with the dimension of time representing the degree of shear-thinning. This model reduces to the Newtonian one for $\eta_0=\eta_\infty$ or $\lambda=1$ so that $\mu(\dot{\gamma})$ becomes constant. The present approximation of a three-parameter shear-thinning model characterizing the complexity in blood rheology indicates that the apparent viscosity as a decreasing function of the shear rate which increases considerably at low shear rates.

While mass transport refers to the movement of atherogenic molecules, that is, blood-borne components, such as oxygen and low-density lipoproteins from flowing blood into the arterial walls or vice versa, the heat transfer relates to the exchange of heat between the arterial wall and the streaming blood by means of which ablative therapies are often applied clinically for treatment of unnatural growth in the arterial lumen. The heat conduction and the convection–diffusion equations governing the flow of heat and mass transport in the blood stream each coupled to the flow velocity-field are also written in dimensionless form as

$$\frac{\partial T}{\partial t}+u\frac{\partial T}{\partial r}+w\frac{\partial T}{\partial z}=\frac{1}{Re.Pr}\left[\frac{\partial^2 T}{\partial r^2}+\frac{1}{r}\frac{\partial T}{\partial r}+\frac{\partial^2 T}{\partial z^2}\right] \tag{6}$$

$$\text{and}\quad \frac{\partial C}{\partial t}+u\frac{\partial C}{\partial r}+w\frac{\partial C}{\partial z}=\frac{1}{Re.Sc}\left[\frac{\partial^2 C}{\partial r^2}+\frac{1}{r}\frac{\partial C}{\partial r}+\frac{\partial^2 C}{\partial z^2}\right], \tag{7}$$

in which the Prandtl number $Pr=\frac{\mu C_p}{k'}$, the Schmidt number $Sc=\frac{\mu}{\rho D}, C_p$ the specific heat, D the coefficient of diffusion, k' the thermal conductivity and the non-dimensional parameters signifying the time, the temperature and the concentration are, respectively, scaled as follows:

$$t\rightarrow\frac{tU_o}{r_o},\quad T\rightarrow\frac{T-T_i}{T_w-T_i},\quad C\rightarrow\frac{C}{C_s}, \tag{8}$$

where r_o is the unconstricted radius of the artery, C_s the reference concentration at the inlet and T_i, T_w are the respective temperatures at the inlet and at the wall.

Three differently shaped models of stenosis having 48% areal occlusion each shown in Fig. 1 have been examined. The first profile of the stenosis considered here is the straight axisymmetric model of Back et al. [30] mimicing real surface irregularities since the actual variation of the cross-sectional area of a left circumflex coronary artery casting from a human cadaver is retained. This stenosis is not symmetric with respect to its narrowest point. The second geometrical model of the stenosis undertaken is the most conventional use of cosine curve, given by

$$R(z)=\begin{cases}1-\frac{\delta}{2r_0}[1+\cos\{\pi(z-z_1)/z_0\}], & 7d\leqslant z\leqslant d+2z_0\\ 1, & \text{otherwise,}\end{cases} \tag{9}$$

where z_0 is the half-length, δ, the maximum width and z_1 is the centre of the stenosis with $\delta=0.276r_0$. Finally, a new stenosis model is investigated similar to the irregular stenosis model having no surface irregularities or roughness elements. Thus this model can be treated as smooth, but in contrast to the cosine-shaped model, the profile of stenosis is no longer symmetric about its narrowest point.

3. Boundary conditions

As the arterial wall is treated to be rigid, the velocity boundary conditions of the blood stream on the wall are the usual no-slip conditions given by

$$w(r,z,t)=0=u(r,z,t)\quad\text{on}\quad r=R(z), \tag{10}$$

while zero transverse velocity gradient and zero cross flow on the axis of symmetry are taken as

$$\frac{\partial w(r,z,t)}{\partial r}=0=u(r,z,t)\quad\text{on}\quad r=0. \tag{11}$$

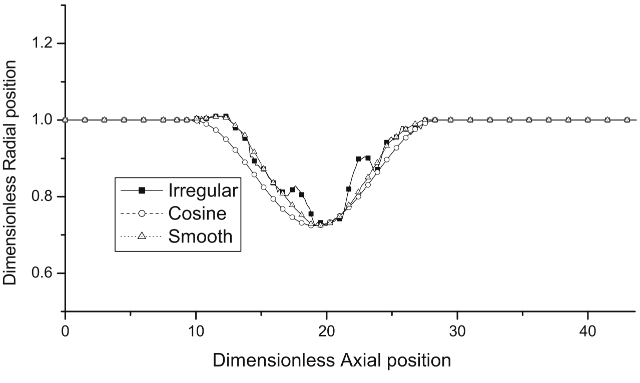

Fig. 1. Comparison of three different stenosis models.

A fully developed pulsatile parabolic velocity profile at the inlet of the stenosed arterial lumen may be assumed as

$$w(r,z,t)=\left(1-\frac{r^2}{R^2}\right)\left[1+ksin\left(\frac{\alpha^2}{Re}t\right)\right] \quad \text{and} \quad u(r,z,t)=0 \quad \text{at } z=0, \tag{12}$$

in which $\alpha=r_0\sqrt{\frac{\omega\rho}{\mu}}$ is the Womersley number while the velocity gradients at the outlet of the arterial segment of finite length L may be taken to be the traction-free conditions as

$$\frac{\partial w(r,z,t)}{\partial z}=0=\frac{\partial u(r,z,t)}{\partial z} \quad \text{at } z=L \quad \text{for } 0\leqslant r\leqslant R(z). \tag{13}$$

The axial symmetry conditions for the temperature and the mass concentration are introduced as

$$\frac{\partial T(r,z,t)}{\partial r}=0=\frac{\partial C(r,z,t)}{\partial r} \quad \text{on } r=0. \tag{14}$$

At the inlet, the mass concentration of the solute is assumed to be constant while the concentration gradient at the outlet may be assumed to be equal to zero, that is, non-dimensionally,

$$C(r,z,t)=1 \quad \text{at } z=0 \quad \text{and} \quad \frac{\partial C(r,z,t)}{\partial z}=0 \quad \text{at } z=L \tag{15}$$

and a Dirichlet boundary condition of the zero-concentration on the arterial wall is set as

$$C(r,z,t)=0 \quad \text{on } r=R(z), \tag{16}$$

which essentially neglects coupling between mass transport in blood and in the arterial wall, that is, zero-concentration on the wall is appropriate when the fluid-side mass transport resistance dominates the wall-side resistance as evident from Ethier [31].

Moreover, the temperature is assumed to be equal to zero at the inlet and a constant temperature is set on the arterial wall so that their non-dimensional representations are, respectively, given by

$$T(r,z,t)=0 \quad \text{at } z=0 \quad \text{and} \quad T(r,z,t)=1 \quad \text{on } r=R(z). \tag{17}$$

4. Radial coordinate transformation

For the purpose of avoiding interpolation error while discretizing the governing equations, we use a suitable coordinate transformation to map the constricted domain into a rectangular one. Eqs. 1, 2 and 3 and 5, 6 and 7 together with the boundary conditions (10)–(17) are transformed by the introduction of a new variable

$$x=\frac{r}{R(z)},$$

as

$$\begin{aligned}\frac{\partial w}{\partial t}=&-\frac{1}{R}\frac{\partial(wu)}{\partial x}-\frac{\partial w^2}{\partial z}+\frac{x}{R}\frac{\partial w^2}{\partial x}\frac{dR}{dz}-\frac{wu}{R}-\frac{\partial p}{\partial z}+\frac{x}{R}\frac{\partial p}{\partial x}\frac{dR}{dz}\\ &+\frac{\mu(\dot{\gamma})}{R^2Re}\left[\left\{1+\left(x\frac{dR}{dz}\right)^2\right\}\frac{\partial^2 w}{\partial x^2}+\left\{\frac{1}{x}+2x\left(\frac{dR}{dz}\right)^2 xR\frac{d^2R}{dz^2}\right\}\right.\\ &\left.\times\frac{\partial w}{\partial x}+R^2\frac{\partial^2 w}{\partial z^2}\right]+\frac{1}{Re}\left[\frac{1}{R}\frac{\partial\mu}{\partial x}\left(\frac{\partial u}{\partial z}-\frac{x}{R}\frac{\partial u}{\partial x}\frac{dR}{dz}+\frac{1}{R}\frac{\partial w}{\partial x}\right)\right.\\ &\left.+2\left(\frac{\partial\mu}{\partial z}-\frac{x}{R}\frac{\partial\mu}{\partial x}\frac{dR}{dz}\right)\left(\frac{\partial w}{\partial z}-\frac{x}{R}\frac{\partial w}{\partial x}\frac{dR}{dz}\right)\right],\end{aligned} \tag{18}$$

$$\begin{aligned}\frac{\partial u}{\partial t}=&-\frac{1}{R}\frac{\partial u^2}{\partial x}-\frac{\partial(wu)}{\partial z}+\frac{x}{R}\frac{\partial(wu)}{\partial x}\frac{dR}{dz}-\frac{u^2}{xR}-\frac{1}{R}\frac{\partial p}{\partial x}\\ &+\frac{\mu(\dot{\gamma})}{R^2Re}\left[\left\{1+\left(x\frac{dR}{dz}\right)^2\right\}\frac{\partial^2 u}{\partial x^2}+\left\{\frac{1}{x}+2x\left(\frac{dR}{dz}\right)^2-xR\frac{d^2R}{dz^2}\right\}\right.\\ &\left.\times\frac{\partial u}{\partial x}-\frac{u}{x^2}+R^2\frac{\partial^2 u}{\partial z^2}\right]+\frac{1}{Re}\left[\frac{2}{R^2}\frac{\partial\mu}{\partial x}\frac{\partial u}{\partial x}+\left(\frac{\partial\mu}{\partial z}-\frac{x}{R}\frac{\partial\mu}{\partial x}\frac{dR}{dz}\right)\right.\\ &\left.\times\left(\frac{\partial u}{\partial z}-\frac{x}{R}\frac{\partial u}{\partial x}\frac{dR}{dz}+\frac{1}{R}\frac{\partial w}{\partial x}\right)\right],\end{aligned} \tag{19}$$

$$xR\frac{\partial w}{\partial z}-x^2\frac{\partial w}{\partial x}\frac{dR}{dz}+\frac{\partial(ux)}{\partial x}=0, \tag{20}$$

$$\begin{aligned}\frac{\partial T}{\partial t}=&-\frac{u}{R}\frac{\partial T}{\partial x}-w\left(\frac{\partial T}{\partial z}-\frac{x}{R}\frac{\partial T}{\partial x}\frac{dR}{dz}\right)+\frac{1}{RePrR^2}\left[\left\{1+\left(x\frac{dR}{dz}\right)^2\right\}\frac{\partial^2 T}{\partial x^2}\right.\\ &\left.+\left\{\frac{1}{x}+2x\left(\frac{dR}{dz}\right)^2-xR\frac{d^2R}{dz^2}\right\}\frac{\partial T}{\partial x}+R^2\frac{\partial^2 T}{\partial z^2}\right],\end{aligned} \tag{21}$$

$$\begin{aligned}\text{and}\quad\frac{\partial C}{\partial t}=&-\frac{u}{R}\frac{\partial C}{\partial x}-w\left(\frac{\partial C}{\partial z}-\frac{x}{R}\frac{\partial C}{\partial x}\frac{dR}{dz}\right)+\frac{\partial C}{\partial t}\frac{1}{ReScR^2}\\ &\times\left[\left\{1+\left(x\frac{dR}{dz}\right)^2\right\}\frac{\partial^2 C}{\partial x^2}+\left\{\frac{1}{x}+2x\left(\frac{dR}{dz}\right)^2-xR\frac{d^2R}{dz^2}\right\}\frac{\partial C}{\partial x}+R^2\frac{\partial^2 C}{\partial z^2}\right],\end{aligned} \tag{22}$$

while the transformed boundary conditions are listed below

$$w(x,z,t)=0=u(x,z,t) \quad \text{on } x=1, \tag{23}$$

$$\frac{\partial w(x,z,t)}{\partial x}=0=u(x,z,t) \quad \text{on } x=0. \tag{24}$$

$$w(x,z,t)=(1-x^2)\left[1+ksin\left(\frac{\alpha^2}{Re}t\right)\right] \quad \text{and} \quad u(x,z,t)=0 \quad \text{at } z=0, \tag{25}$$

$$\frac{\partial w(x,z,t)}{\partial z}=0=\frac{\partial u(x,z,t)}{\partial z} \quad \text{at } z=L, \tag{26}$$

$$\frac{\partial T(x,z,t)}{\partial x}=0=\frac{\partial C(x,z,t)}{\partial x} \quad \text{on } x=0, \tag{27}$$

$$C(x,z,t)=1 \quad \text{at } z=0 \quad \text{and} \quad \frac{\partial C(x,z,t)}{\partial z}=0 \quad \text{at } z=L, \tag{28}$$

$$C(x,z,t)=0 \quad \text{and } T(x,z,t)=1 \quad \text{on } x=1, \tag{29}$$

$$\text{and} \quad T(x,z,t)=0 \quad \text{at } z=0. \tag{30}$$

5. The MAC methodology

The above governing equations along with the set of initial and boundary conditions including the non-zero initial conditions are solved numerically by finite-difference method with non-uniform grid in both the axial and the radial directions. Control volume-based finite-difference discretization of those equations is carried out in staggered grid. In this type of grid alignment, the flow velocity-field and the pressure are calculated at different locations of the control volume as indicated in Fig. 2 while the difference equations have been derived in three distinct cells corresponding to the continuity equation (20), the axial momentum (18) and the radial momentum (19) equations. The difference equations corresponding to the heat conduction (21) and the convection–diffusion equation (22) have also been derived accordingly. The discretizations of the time derivative terms are based on the first order accurate two-level forward time differencing formula while those for the convective terms in the momentum equations are accorded with a hybrid formula consisting of central differencing and second order upwinding. The diffusive terms are, however, discretized by second order accurate three-point central difference formula. Thus in a finite-difference formula with $x=j\delta x_j, z=i\delta z_i, t=n\delta t$ and $p(x,z,t)=p(j\delta x_j, i\delta z_i, n\delta t)=p^n_{i,j}$ in which n refers to the time direction, δt, the time increment and $\delta z_i, \delta x_j$ are the respective width and length of the (i,j)th cell of the control volume. The discretized version of the continuity equation (20) at the (i,j) cell becomes

$$\begin{aligned}&\frac{x_jR_i}{\delta z_i}\left(w^n_{i+\frac{1}{2},j}-w^n_{i-\frac{1}{2},j}\right)-\frac{(x_j)^2}{\delta x_j}\left(w^n_{i,j+\frac{1}{2}}-w^n_{i,j-\frac{1}{2}}\right)\left(\frac{dR}{dz}\right)_i\\ &\quad+\frac{1}{\delta x_j}\left(x_{j+\frac{1}{2}}u^n_{i,j+\frac{1}{2}}-x_{j-\frac{1}{2}}u^n_{i,j-\frac{1}{2}}\right)=0.\end{aligned} \tag{31}$$

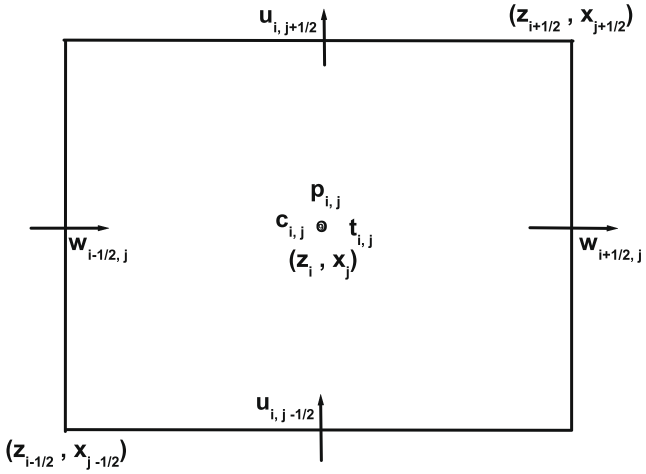

Fig. 2. A typical MAC cell.

Here, (z_i, x_j) and $\left(z_{i+\frac{1}{2}}, x_{j+\frac{1}{2}}\right)$ represent the respective co-ordinates >of the cell centre and the cell top right corner of the (i,j)th control volume (cf. Fig. 2). Considering the source, convective and diffusion terms at the nth time level, the momentum equation in z-direction may be put to the form

$$\frac{w^{n+1}_{i+\frac{1}{2},j} - w^{n}_{i+\frac{1}{2},j}}{\delta t} = \frac{p^n_{i,j} - p^n_{i+1,j}}{0.5(\delta z_i + \delta z_{i+1})} + \frac{x_j}{R_{i+\frac{1}{2}}}\left(\frac{dR}{dz}\right)_{i+\frac{1}{2}} \times \frac{\left(p^n_{i+\frac{1}{2},j+\frac{1}{2}} - p^n_{i+\frac{1}{2},j-\frac{1}{2}}\right)}{\delta x_j} + (w_{me})^n_{i+\frac{1}{2},j}, \tag{32}$$

in which $p^n_{i+\frac{1}{2},j+\frac{1}{2}}$ and $p^n_{i+\frac{1}{2},j-\frac{1}{2}}$ designate the pressure at the top and the bottom positions of the right face of MAC cell, respectively, while $(w_{me})^n_{i+\frac{1}{2},j}$ consists of the convective, the diffusive and the viscous dissipative terms of the w-momentum at the nth time level at (i,j) cell, the expression of which is not presented for the sake of brevity.

Likewise the finite-difference equation approximating the momentum equation in x-direction is given by

$$\frac{u^{n+1}_{i,j+\frac{1}{2}} - u^{n}_{i,j+\frac{1}{2}}}{\delta t} = \frac{1}{R_i}\frac{\left(p^n_{i,j} - p^n_{i,j+1}\right)}{0.5(\delta x_{j+1} + \delta x_j)} + (u_{me})^n_{i,j+\frac{1}{2}}, \tag{33}$$

where $(u_{me})^n_{i,j+\frac{1}{2}}$ comprises of the convective, the diffusive and the viscous dissipative terms of the u-momentum equation at the nth time level at (i,j) cell.

The Poisson equation for pressure, derived from the Eqs. (31)–(33) takes the final form as

$$\begin{aligned}\frac{Div^{n+1}_{i,j} - Div^n_{i,j}}{\delta t} &= A_{i,j}p^n_{i,j} + B_{i,j}p^n_{i+1,j} + C_{i,j}p^n_{i-1,j} + D_{i,j}p^n_{i,j+1} \\ &\quad + E_{i,j}p^n_{i,j-1} + F_{i,j}p^n_{i+1,j+1} + G_{i,j}p^n_{i+1,j-1} \\ &\quad + H_{i,j}p^n_{i-1,j-1} + S_{i,j}p^n_{i-1,j+1} \\ &\quad + \frac{x_jR_i}{\delta z_i}\left[(w_{me})^n_{i+\frac{1}{2},j} - (w_{me})^n_{i-\frac{1}{2},j}\right] \\ &\quad + \frac{1}{\delta x_j}\left[x_{j+\frac{1}{2}}(u_{me})^n_{i,j+\frac{1}{2}} - x_{j-\frac{1}{2}}(u_{me})^n_{i,j-\frac{1}{2}}\right].\end{aligned} \tag{34}$$

Here, $Div^n_{i,j}$ represents the discretized form of the divergence of velocity-field at the (i,j) cell and the expressions for $A_{i,j}, B_{i,j}, \ldots, H_{i,j}, S_{i,j}$ have got their respective expressions included in Appendix A.

The advantage in using MAC cell is that the pressure boundary condition is not needed at the boundaries where the velocity vector is specified, because the domain boundaries are chosen to fall on velocity nodes. The Poisson equation for pressure (34) is solved by Successive Over Relaxation (SOR) method with the chosen value of over relaxation parameter as 1.2. After having determined the flow velocity-field using pressure duly obtained, the temperature and the mass concentration can easily be evaluated from the following respective discretized versions of the Eqs. (21) and (22) accompanied by the relevant boundary conditions (27)–(30) as

$$\begin{aligned}\frac{T^{n+1}_{i,j} - T^n_{i,j}}{\delta t} = &-\frac{u^n_{i,j}}{R_i}\left(\frac{\partial T}{\partial x}\right)^n_{i,j} - w^n_{i,j}\left\{\left(\frac{\partial T}{\partial z}\right)^n_{i,j} - \frac{x_j}{R_i}\left(\frac{\partial T}{\partial x}\right)^n_{i,j}\left(\frac{dR}{dz}\right)_i\right\} \\ &+ \frac{1}{RePrR_i^2}\left[\left[1 + \left\{x_j\left(\frac{dR}{dz}\right)_i\right\}^2\right]\left(\frac{\partial^2 T}{\partial x^2}\right)^n_{i,j}\right. \\ &+ \left\{\frac{1}{x_j} + 2x_j\left[\left(\frac{dR}{dz}\right)_i\right]^2 - x_jR_i\left(\frac{d^2R}{dz^2}\right)_i\right\}\left(\frac{\partial T}{\partial x}\right)^n_{i,j} \\ &\left.+ (R_i)^2\left(\frac{\partial^2 T}{\partial z^2}\right)^n_{i,j}\right],\end{aligned} \tag{35}$$

and

$$\begin{aligned}\frac{C^{n+1}_{i,j} - C^n_{i,j}}{\delta t} = &-\frac{u^n_{i,j}}{R_i}\left(\frac{\partial C}{\partial x}\right)^n_{i,j} - w^n_{i,j}\left\{\left(\frac{\partial C}{\partial z}\right)^n_{i,j} - \frac{x_j}{R_i}\left(\frac{\partial C}{\partial x}\right)^n_{i,j}\left(\frac{dR}{dz}\right)_i\right\} \\ &+ \frac{1}{ReScR_i^2}\left[\left[1 + \left\{x_j\left(\frac{dR}{dz}\right)_i\right\}^2\right]\left(\frac{\partial^2 C}{\partial x^2}\right)^n_{i,j}\right. \\ &\left.+\left\{\frac{1}{x_j} + 2x_j\left[\left(\frac{dR}{dz}\right)_i\right]^2 - x_jR_i\left(\frac{d^2R}{dz^2}\right)_i\right\}\left(\frac{\partial C}{\partial x}\right)^n_{i,j} + (R_i)^2\left(\frac{\partial^2 C}{\partial z^2}\right)^n_{i,j}\right].\end{aligned} \tag{36}$$

6. Pressure and velocity corrections

In most of the codes based on staggered grid formulations, the local dilation term at the $(n+1)$th time level, $Dil^{n+1}_{i,j}$, is set equal to zero. Here we replace the term

$$Dil^{n+1}_{i,j} = \frac{x_jR_i}{\delta z_i}\left(w^{n+1}_{i+\frac{1}{2},j} - w^{n+1}_{i-\frac{1}{2},j}\right) + \frac{1}{\delta x_j}\left(x_{j+\frac{1}{2}}u^{n+1}_{i,j+\frac{1}{2}} - x_{j-\frac{1}{2}}u^{n+1}_{i,j-\frac{1}{2}}\right)$$

by $\frac{(x_j)^2}{\delta x_j}\left(w^n_{i,j+\frac{1}{2}} - w^n_{i,j-\frac{1}{2}}\right)\left(\frac{dR}{dz}\right)_i$,

where $w^n_{i,j+\frac{1}{2}}$ and $w^n_{i,j-\frac{1}{2}}$ are at the nth time level, in order to obtain the exact form of the transformed continuity equation in the Poisson equation for pressure, so that the decoupled tendency of pressure-field gets eliminated. With this incorporation, the pressure equation becomes independent of $(n+1)$th time level velocity-field. For large number of grid points, very large number of iteration steps is needed for satisfactory level of convergence. To reduce the computation time for each cycle, the number of iterations in the SOR iteration scheme is kept limited to 10. But the convergence of pressure solutions cannot be expected with such a small number of iterations. So the velocity-field obtained after solving the momentum equations using an already known inaccurate pressure-field may not satisfy the continuity equation. This necessitates a corrector stage. In this stage the pressure and subsequently the velocities are corrected to get more improved values in the sense that the velocity-field will satisfy the continuity equation more accurately. The second stage starts with computing the divergence of velocity-field for each cell. If the tolerance is found to be greater than 0.5×10^{-12} at any cell in absolute sense, the pressure is immediately corrected for each cell in the flow-field. The velocity components at the sides of the cell are then adjusted accordingly. The pressure correction formula is

$$p_{i,j}^{n} = p_{i,j}^{\star} + \omega\delta p_{i,j}, \tag{37}$$

where $p_{i,j}^{\star}$ is obtained after solving the Poisson equation, $\omega(\leqslant 0.5)$ is an under-relaxation parameter and

$$\delta p_{i,j} = -\frac{Div_{i,j}^{\star}}{\delta t A_{i,j}},$$

where $Div_{i,j}^{\star}$ is the value of the divergence of velocity-field at the cell (i,j) obtained after solving the Poisson equation for pressure. The velocity correction formulae are consequently given by

$$w_{i+\frac{1}{2},j}^{n+1} = w_{i+\frac{1}{2},j}^{\star} + \frac{\delta t\delta p_{i,j}}{0.5(\delta z_i + \delta z_{i+1})},$$

$$w_{i-\frac{1}{2},j}^{n+1} = w_{i-\frac{1}{2},j}^{\star} - \frac{\delta t\delta p_{i,j}}{0.5(\delta z_i + \delta z_{i-1})},$$

$$u_{i,j+\frac{1}{2}}^{n+1} = u_{i,j+\frac{1}{2}}^{\star} + \frac{1}{R_i}\frac{\delta t\delta p_{i,j}}{0.5(\delta x_{j+1} + \delta x_j)},$$

$$u_{i,j-\frac{1}{2}}^{n+1} = u_{i,j-\frac{1}{2}}^{\star} - \frac{1}{R_i}\frac{\delta t\delta p_{i,j}}{0.5(\delta x_j + \delta x_{j-1})},$$

where $w_{i+\frac{1}{2},j}^{\star}, w_{i-\frac{1}{2},j}^{\star}, u_{i,j+\frac{1}{2}}^{\star}$ and $u_{i,j-\frac{1}{2}}^{\star}$ represent the updated velocity-field.

7. Numerical stability

Amsden and Harlow [32] suggested that the number of calculation cycles and hence the running time could be reduced by the use of an adaptive time stepping routine which, at a given cycle, would automatically choose the time step most appropriate to the velocity-field at that cycle. Welch et al. [33] discussed the stability and accuracy requirements for the MAC method. They suggested that two stability restrictions are required. The first is akin to the Courant condition which will only be appropriate for selected class of problems. The second stability restriction involves the Reynolds number:

$$\delta t_1 \leqslant Min\left[\frac{Re}{2}\frac{\delta z_i^2\delta x_j^2}{\delta z_i^2 + \delta x_j^2}\right]_{i,j}. \tag{38}$$

This stability condition is related to viscous effect (cf. Hirt [34]) which can be applied directly to select an appropriate time step.

A more appropriate treatment used by Markham and Proctor [35], among others, is to require that no particles should cross more than one cell boundary in a given time interval that is,

$$\delta t_2 \leqslant Min\left[\frac{\delta z_i}{|w|}, \frac{\delta x_j}{|u|}\right]_{i,j}. \tag{39}$$

We now discuss the implementation of this adaptive time-stepping procedure. The time step to be used at a given point in the calculation will be

$$\delta t = a\, Min[\delta t_1, \delta t_2], \tag{40}$$

where $0 < a \leqslant 1$; the reason for this extra added factor a in (40) led to a considerable computational savings as evident from [35] and our experience concurs with them.

Moreover, the upwinding parameter β appearing in the expression of $(w_{me})_{i+\frac{1}{2},j}^{n}$ is selected according to the inequality

$$1 \geqslant \beta \geqslant \text{Max}\left[\frac{|w\delta t|}{\delta z_i}, \frac{|u\delta t|}{\delta x_j}\right]_{i,j}.$$

This inequality yields a small value of the parameter β. As a safety measure the value is multiplied by a factor 1.2, in practice.

8. Numerical results and discussion

Numerical computation of the desired quantities having major physiological significance are primarily based upon the following parameters obtained from [30,36]: $\alpha = 2, Re = 300, Pr = 0.72, Sc = 3, k = 0.1, \lambda = 40, \wedge = 50, r_o = 0.154\,\text{cm}, \rho = 1.05 \times 10^3\,\text{kg}\quad \text{m}^{-3}$ and $L = 43.6$.

The computational domain has been confined with a finite non-dimensional arterial length of 43.6 in which the upstream and downstream lengths have been selected to be 8 and 15 times the unconstricted non-dimensional radius, respectively. For this computational domain, solutions are computed through the generation of staggered grid with a size of 652 × 50 while the insertion of additional points whatsoever needed between any two consecutive original irregular stenosis data of Back et al. [30] by interpolation has been made for the purpose of generating finer mesh adequately. The governing equations of motion are solved numerically using the pressure based finite-difference approximation. The grid-independence study is made for the verification of the present numerical scheme. The w-velocity at different ordinates in a straight tube at the outlet are compared with the exact solution at Reynolds number 300 as shown in Table 1. This shows good agreement between exact values of w-velocity and the computational values of w-velocity obtained from different grid sizes for a straight tube.

An extensive quantitative analysis has been performed for various physical quantities of major physiological relevance such as the velocity profiles, the pressure drop, the patterns of stream lines, the wall shear stress, the profiles of temperature distribution, the mass concentration and the distribution of local Sherwood number through each of the stenosis models together with their detailed comparisons as well have also been made with the existing theoretical and experimental results.

The results of the predicted pressure drop across three different stenosis models distributed over various severity of constrictions in terms of percentage cross-sectional area reduction resulting in mild, moderate and severe stenosis in the genesis of atherosclerosis are presented in Fig. 3 at the same instant of $t = 100$ for $Re = 300$. The curves of this figure based on various types of constrictions corresponding to irregular, cosine and smooth stenosis appear to follow the increasing trend gradually with increasing percentage of area reduction, that means, more the severity of the stenosis more the amount of pressure drop. One may record from the present results that the pressure drop appears significantly higher in the case of cosine shape of the stenosis and moderately higher for smooth stenosis with respect to the irregular

Table 1
Results of velocity for different grid sizes in a straight tube (Newtonian fluid model).

Grid	Property	$x = 0$	$x = 0.19347$	$x = 0.42278$	$x = 0.61396$	$x = 0.80502$	$x = 1$
652 × 50	w	1.0	0.9625369	0.8212349	0.6230387	0.3519528	0
Exact	$1 - x^2$	1.0	0.9625694	0.8212571	0.6230531	0.3519428	0
			$x = 0.22193$	$x = 0.40254$	$x = 0.61171$	$x = 0.80994$	
652 × 40	w	1.0	0.9506867	0.8379124	0.6257994	0.3440178	0
Exact	$1 - x^2$	1.0	0.9507471	0.8379615	0.6258109	0.3439972	0

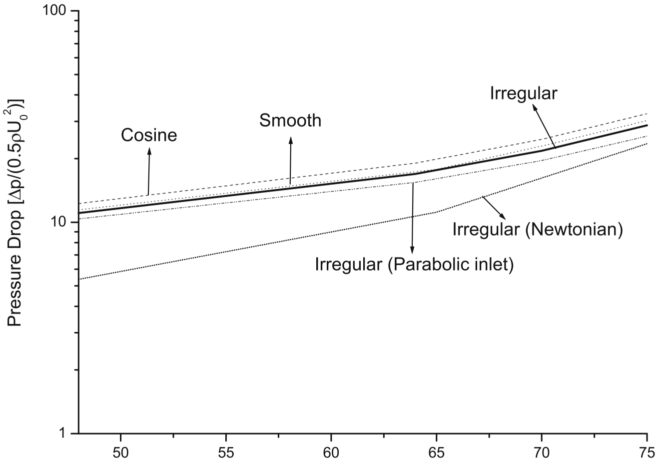

Fig. 3. Comparison of nondimensional pressure drop acros three different stenosis models at $t = 100$.

one. This happens due to the variance of the area covering of the different models of the stenosis under consideration. It may be noted that the respective area covering of 31.20% and 7.23% more in the cosine and smooth stenosis with respect to the irregular one helps enhancing the pressure drop. The present observation agrees well with that of Yakhot et al. [37] that the excess pressure drop is neither caused by the smoothness of the stenosis nor by its higher degree of symmetry relative to the irregular stenosis but is rather an effect of area covering with respect to the irregular stenosis though their studies were based on Newtonian flow past a stenosed artery. Here too, the influence of the non-Newtonian rheology and parabolic inlet flow condition is well reflected on the pressure drop in the case of irregular stenosis where the pressure drop declines uniformly from that of non-Newtonian and parabolic inlet one, as anticipated and eventually the velocity of the flow diminishes as evident from Fig. 4.

Fig. 4 exhibits the variation of the axial velocity profiles of the streaming blood along the radial direction for each of the stenosis models with 48% area reduction at the throat of the stenosis indicating a border line between moderate and severe stenosis at a specific instant of $t = 100$. It appears from the results of the present figure that although the nature of the velocity profile corresponding to three different stenoses remains analogous to some extent but the velocity corresponding to irregular stenosis predicts lower values than those of cosine and smooth ones until a radial position of 0.82 and beyond which, that is, in the vicinity of the arterial wall they are considerably reversed. The deviation of the results thus obtained indicates the relative quantitative measure of the effects of different stenosis models on the velocity profiles. It is obvious from the present figure that velocity profile becomes more parabolic in case of Newtonian model. The present figure further includes how the velocity profile in the case of irregular stenosis gets influenced by the parabolic inlet ($k = 0$). The inclusion of parabolic inlet condition instead of pulsatile one causes uniform reduction of the velocity over the entire arterial cross-section at the narrowest location. While most of the previous work have been limited to steady flow only, the present study does incorporate the effect of flow unsteadiness on the velocity profile and that can be estimated quantitatively through a direct comparison of the second and third curves from the bottom of the present figure. Since there is a coupling between the growth of the stenosis and the arterial flow of blood each affecting the other significantly and since the development of arterial narrowing usually of varied geometrical shapes, the choice of differently shaped stenosis models considered herein underlines its own importance in the atherosclerotic flow analysis.

The narrowest passage of all the outlines of the irregular, cosine, smooth stenosis and the Newtonian fluid past irregular stenosis and their implications on the flow velocity give rise to higher wall shear stress in the converging regions of the stenosis, as depicted in Fig. 5 corresponding to 64% area reduction for $Re = 300$. Here, the wall shear stress has been normalised by its magnitudes in the unconstricted tube far upstream the stenosis. In the converging section of the stenosis, the irregular stenosis model predicts lower shear stress values from those of cosine and smooth stenosis models but at the throat of the stenosis, values are much higher followed by a drop from higher shear stress to lower shear stress in the diverging section of the stenosis. This observation of the nature of the wall shear stress distribution over the entire arterial segment is quite consistent with the findings of Johnston and Kilpatrick [38], Andersson et al. [39] and Yakhot et al. [37]. The present figure also records that there are three separation zones for Newtonian fluid whereas no separation zones occur for generalized Newtonian rheology of fluid.

While the results of Fig. 6a at $Re = 300$ represent the qualitative measure of the effect of Womersley parameter on the temperature profiles for a moderate irregular stenosis with 48% area reduction, the profiles of Fig. 6b for exhibit how they are being influenced significantly by the non-Newtonian rheology of the streaming blood. Fig. 6c illustrates the behaviour of the temperature profiles under

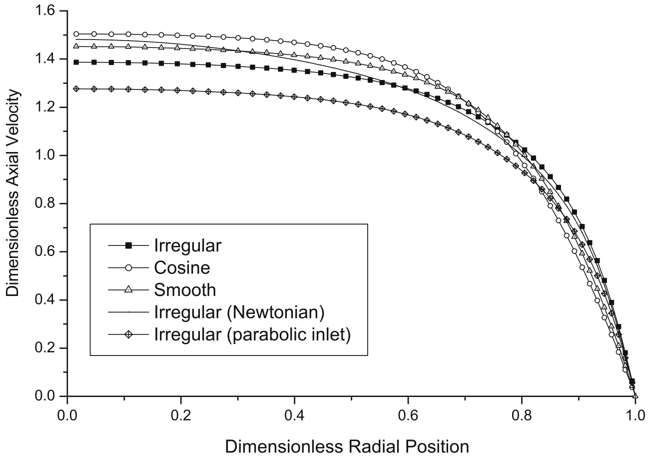

Fig. 4. Axial velocity profiles for each of the stenosis models with 48% area reduction at the throat of the stenosis at $t = 100$.

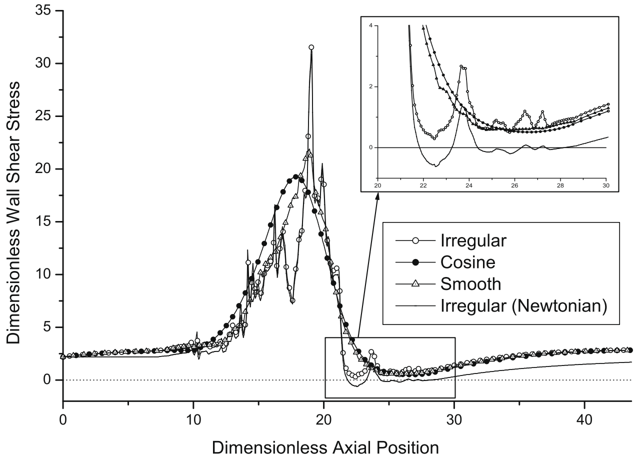

Fig. 5. Variation of normalized wall shear stress through each of the stenosis models with 64% area reduction.

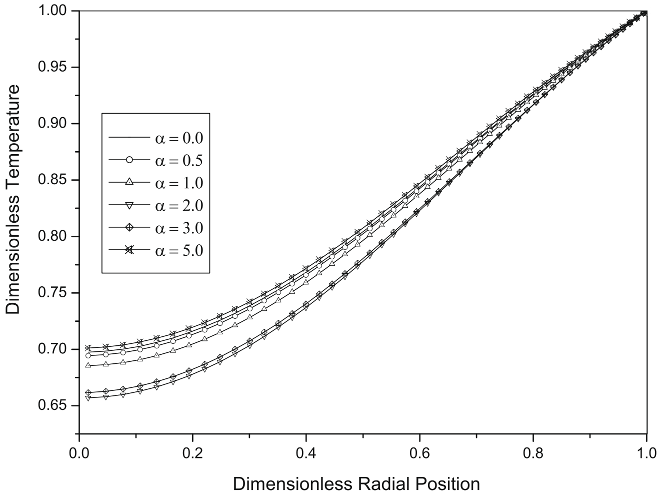

Fig. 6a. Profiles of the temperature for irregular stenosis with $k = 0.1\%$ and 48% area reduction at $Re = 300$.

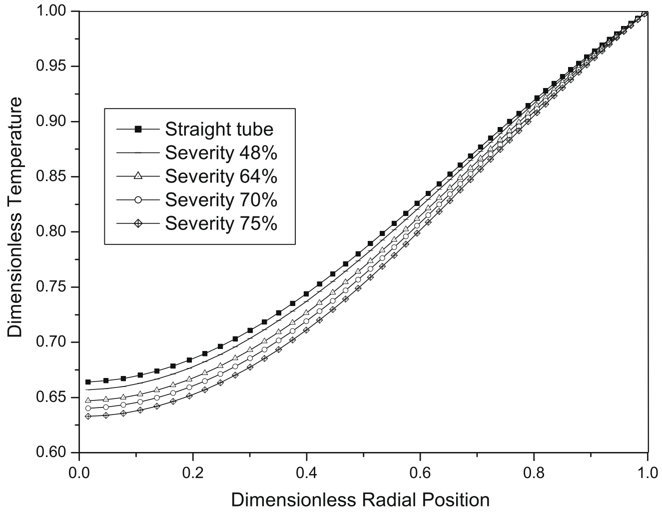

Fig. 6c. Profiles of the temperature based on stenosis-severity for irregular stenosis with $k = 0.1$ and $\alpha = 2$ at $Re = 300$.

stenotic condition for irregular stenosis having severity ranging from 48% to 75% occlusion for $\alpha = 2$ at the same *Re*. The effects of non-Newtonian idealisation of blood and of the introduction of the parabolic inlet flow on the temperature distribution over the entire arterial segment are quantified in Fig. 6d for the same *Re*. More intensively, the various temperature profiles corresponding to different locations of the constricted artery are also explored in Fig. 6e when the artery assumes 48% severity of the stenosis. Examining the results of the present figures several observations deserve attention from the physiological point of view and hence can be recorded. As the pulsatile axial velocity produces a pulsating temperature profile, Fig. 6a shows that although the curves do shift towards the origin with increasing α for 0.0–2.0 but the profiles shift away from the origin with increasing α for 3.0–5.0. The sizable deviation of the temperature profile more towards the axis of the artery may be noticed in Fig. 6b in order to estimate the quantitative effect of generalized Newtonian characterization of the fluid and the magnitudes of temperature get enhanced for generalized Newtonian fluid over those of Newtonian one. The temperature appears to drop gradually from its maximum value for a straight tube with increasing severity of the stenosis, that is, more the severity of the constriction less the temperature as evident from Fig. 6c. The introduction of the parabolic inlet flow condition causes temperature to be largely distributed over the entire arterial segment than that for a pulsatile one under consideration as evident from Fig. 6d. Moreover, Fig. 6e represents the cross-sectional profiles of the temperature distribution at various location of the stenosed arterial segment for irregular model of the stenosis having 48% area reduction at the same $Re = 300$. It appears from this figure that the analogous behaviour of the three consecutive curves at the bottom represents the distribution of the temperature in the proximal of the irregular stenosis. But the profile gets deviated downstream the constriction, that is, in the diverging section ($z = 25.02$) of the stenosis where back flow occurs and recirculation zones are formed as noted earlier. At this critical location, the temperature distribution profile appears to have a point of inflexion unlike others while two remaining profiles at the top show the distribution of temperature at the offset ($z = 30.05$) of the stenosis and at the exit ($z = 40.05$) of the arterial segment. Of considerable interest in studying the wall tissue thermal interactions is the convective heat transfer at the exit of the arterial tube, which describes the amount of energy carried out by the streaming blood that perfuses the tissue. Examining all the results of the present figure one may note that the centre lamina is greatly involved in the heat transfer

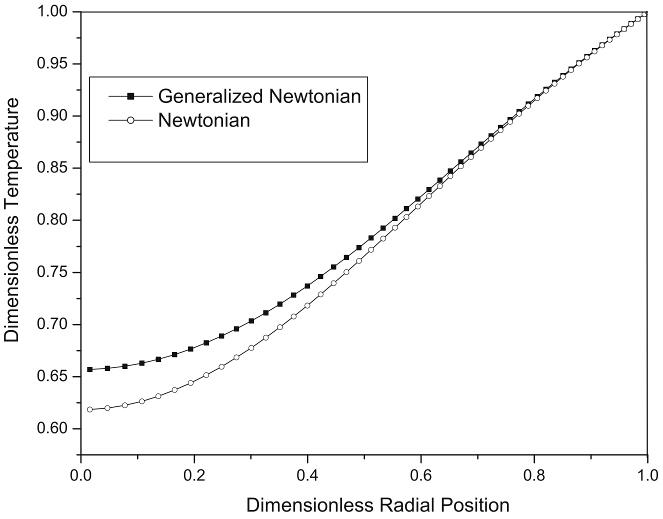

Fig. 6b. Profiles of the temperature for irregular stenosis with 48 % area reduction for $k = 0.1$ and $\alpha = 2$ at $Re = 300$.

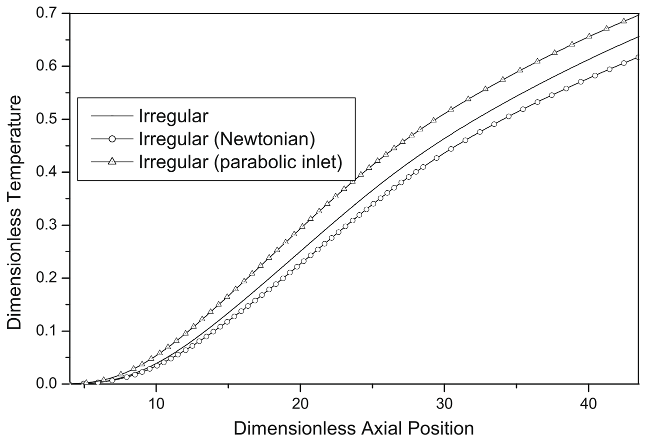

Fig. 6d. Temperature distribution profiles for irregular stenosis with 48% area reduction at $Re = 300$.

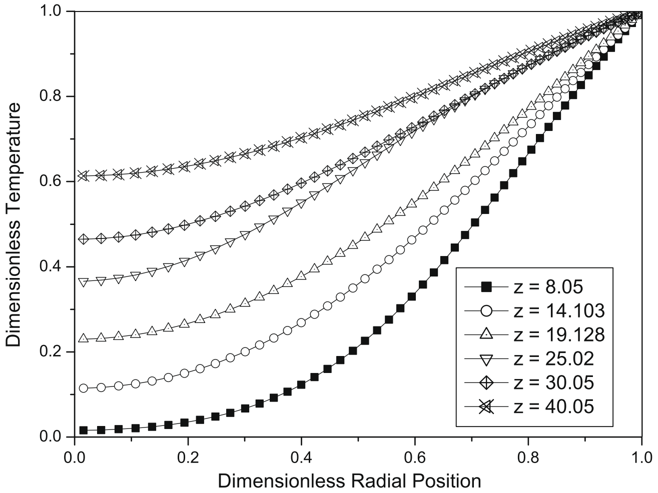

Fig. 6e. Profiles of the temperature at various locations of the stenosed artery with 48% area reduction at *Re* = 300.

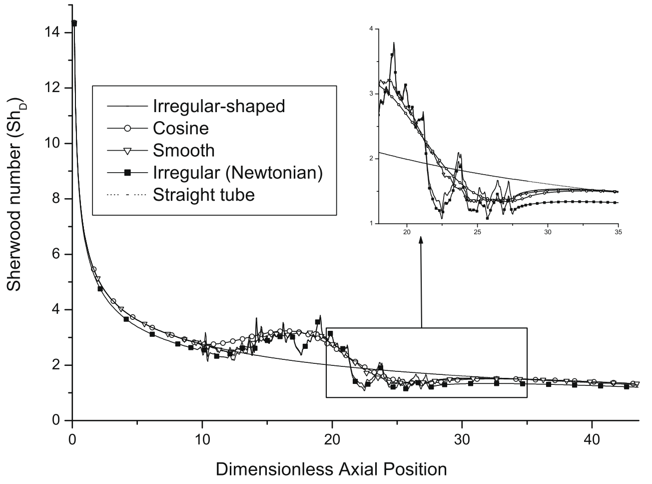

Fig. 7a. Distribution of local Sherwood number through each of the stenosis models with 48% area reduction.

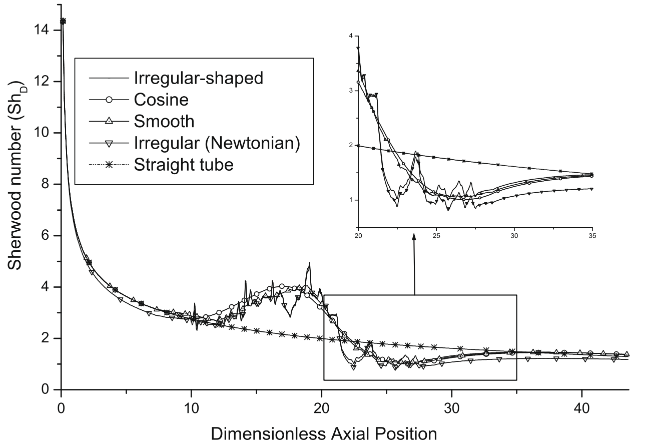

Fig. 7b. Distribution of local Sherwood number through each of the stenosis models with 64% area reduction.

mechanism and thermal equilibration with the arterial wall tissues may be illustrated by the fact that the radial temperature profile at the exit is relatively closer to the arterial wall temperature. The present results appear to be consistent with those of Craciunescu and Clegg [40] who also analyzed the effects of pulsatile blood flow on temperature distribution and heat transfer in rigid vessels with Newtonian fluid idealisation of blood.

For a more quantitative insight into the patterns of mass transport in three different models of stenosis, the distributions of Sherwood number (Sh_D) over the entire stenosed arterial segment are finally examined for two different severity of stenosis in Fig. 7a and b. Generally, the mass flux to the arterial wall may be quantified through the Sherwood number defined by $Sh_D = \frac{nd}{D\Delta C}$, where n is the local mass flux to the arterial wall, d the inlet diameter of the artery and ΔC is a reference concentration difference, that is, the difference between inlet concentration and the wall concentration. The local mass flux (n) has been computed by numerical differentiation of the concentration gradient at the arterial wall. Both the figures are also accompanied by the Sh_D distribution corresponding to a straight tube free from any constriction in its lumen in order to estimate the effect of constrictions of varied nature on the Sh_D number, the key parameter in the mass transport phenomena. One may observe from the features of these figures that the Sh_D distributions right from the inlet section to the onset of stenosis at ($z = 10$) are very well consistent with those of straight tube but considerable deviations depending upon the different stenosis models may be recorded with respect to constriction-free arterial tube. The maximum mass transfer rate occurs slightly upstream of the stenosis throat like the case of the peak wall shear stress shown in Fig. 5. The enhancement of Sh_D or the occurrence of maximum shear stress in the constricted region causes damage of the endothelial cells resulting the increasing permeability of the stenosed wall where the mass particles dissolved in fluid representing blood are deposited most. The minimum value of Sh_D is less than 1 occurring at the low velocity region downstream the constriction and the Sherwood number keeps on increasing to approach finally the distribution for a non-constricted artery. Again the present results do agree qualitatively well with those of Kaazempur-Mofrad et al. [7]. The deviation of the results corresponding to the present consideration of different models of stenosis clearly estimates the influence of individual geometry of the stenosis on the mass flux to the arterial wall. Also the severity of the stenosis causes the maximum and minimum values of Sh_D to change appreciably and the deviation is larger with respect to non-stenotic artery when the severity of the stenosis is allowed to increase in terms of increasing percentage of the cross-sectional area reduction.

The cross-sectional profiles of the mass concentration corresponding to different axial positions of the stenotic and non-stenotic regions for irregular model of stenosis having area reduction of 48% are displayed in Fig. 8 for $Re = 300$. The general observation is that the concentration patterns follow the outline of the flow velocity as anticipated. It appears that the profiles get distorted substantially downstream the throat of the stenosis ($z = 25.02, 30.05$) where flow separation zones are formed while nearly parabolic profile is retained in the flow upstream. Along the upstream side of the stenosis both the flow velocity and the wall shear stress increase as the flow gets accelerated towards the throat, there is a decreasing mass concentration of the solute. These observations are generally consistent also with experimental measurements of labeled cholesterol uptake in excised arterial segments conducted by Deng et al. [41]. All these results suggest besides the role of wall shear stress, another possible role for mass transfer effects in the enlargement of pre-existing arterial stenoses and one may predict that stenoses should grow further distal to the throat of the stenosis.

Finally, the concluding Fig. 9 shows the computed patterns of streamlines through the arterial lumen having three different types of stenosis with 75% area reduction at an instant of $t = 100$. These

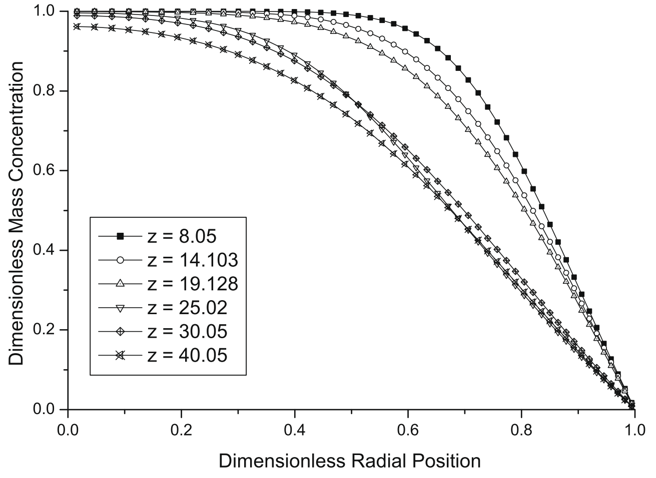

Fig. 8. Profiles of the mass concentration for irregular stenosis with 48% area reduction.

patterns include flow separation downstream the constriction, that is, just distal to the throat of the stenosis and the formation of separation zones distal to the stenosis for Newtonian model. This feature is well agreed with the observation of Stangeby and Either [42]. The streamlines for irregular stenosis model appear to be much more complex in terms of the formation of several recirculation zones downstream the stenosis which may be justified that as the flow approaches towards the throat of the constriction, the axial flow streamlines curve appears to follow the outline of the stenosed wall with the induction of a transverse pressure gradient and a corresponding secondary flow. This causes the formation of several flow separation zones in the diverging section of the stenosis resulting in the appearance of complex recirculation zones on the stenosed arterial wall and eventually the streamlines recover normally much further downstream, distal to stenotic region. Thus studying the distinctive features of the streamlines, one may note that the irregular stenosis present in the arterial lumen affects the streamlines most compared to the cosine stenosis model and hence care needs to be exercised for the irregular stenosis model leading to atherosclerotic lesion. The present findings are also in good agreement with those of Kaazempur-Mofrad et al. [7] who studied mass transport and fluid flow in both axisymmetric and asymmetric stenosis models.

9. Concluding remarks

An updated arterial model based on both the heat and the mass transfer to the streaming blood (non-Newtonian) past three different types of stenosis (axisymmetric, asymmetric) in its lumen is proposed in the current study. The arterial stenosis with 48%, 64% and 75% cross-sectional area reduction is represented by mild, moderate and severe stenosis, respectively, occurring at different stages of the development of atherosclerotic disease. This study records that the patterns of the flow, the heat and the mass transfer, the pressure drop, the wall shear stress and the Sh_D number are strongly dependent on the shape of the stenosis in addition to the non-Newtonian rheology of blood in general, and the irregular shape having closer physiological relevance, in particular.

Although there are some similarities between the models of the stenosis regarding their responses to the heat and the mass transport phenomena, there is a general tendency of the occurrence of flow separation zones downstream of the stenosis, that is, of the mass transport boundary layer to thicken at the specific site distal to the throat of the stenosis. However, these models differ in their both heat flow and mass transfer patterns in the immediate neigh-

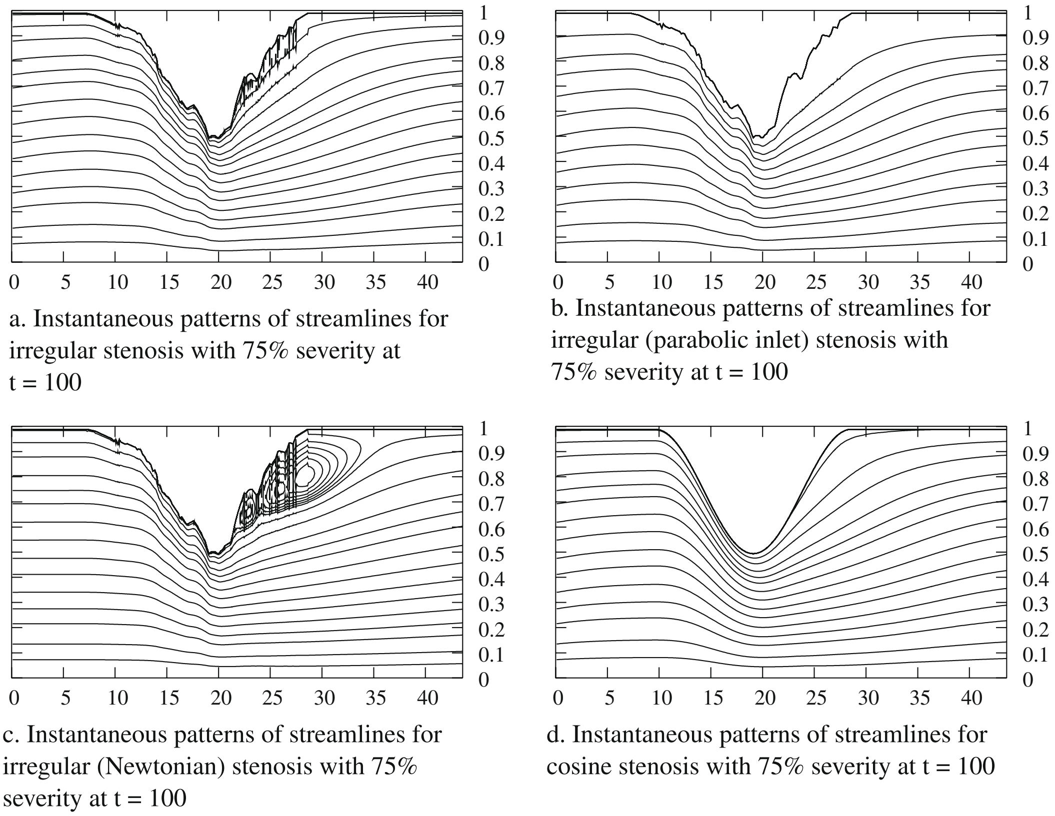

a. Instantaneous patterns of streamlines for irregular stenosis with 75% severity at t = 100

b. Instantaneous patterns of streamlines for irregular (parabolic inlet) stenosis with 75% severity at t = 100

c. Instantaneous patterns of streamlines for irregular (Newtonian) stenosis with 75% severity at t = 100

d. Instantaneous patterns of streamlines for cosine stenosis with 75% severity at t = 100

Fig. 9. Comparison of the patterns of streamlines for different conditions and geometry.

bourhood and distal to the stenosis. In the irregular stenosis model featuring diseased artery in the realm of the genesis of atherosclerosis, the emergence of downstream secondary flow features contributed to circumferentially non-uniform mass concentration profile and to the temperature profile that are different from those in cosine and smooth stenosis models, the concept of the mechanism of bioheat transfer is necessary to model the hyperthermia-induced temperature distribution. The best exchange between the living tissues and the blood network that passes through it depends on the geometry of the blood vessel, the nature of blood flow and the biomechanical properties of blood and the surrounding tissues. The present temperature profiles distributed over the various locations of the stenosed artery may have some implications in hyperthermia in a way to initiate and help develop more accurate models of ablative therapies and improve ablation procedures.

The key results of the present study indicate that the presence of stenosis makes the diseased artery function in a direction which is opposite to that of healthy normal one free from any constriction. The occurrence of high wall shear stress and the maximum Sherwood number at the throat of the stenosis in the formation of atherosclerosis can imply more damage as plaque disruptions. Moreover, the formation of several recirculation zones in the downstream vicinity from the stenosis can allow the disease to develop further creating new intimal thickening. Thus the combined effect of heat and mass transfer on non-Newtonian idealisation of the streaming blood indicates a gateway to draw linkage to atherosclerosis.

Acknowledgements

The authors thankfully acknowledge the suggestions from the reviewers while revising the manuscript. The present work is part of the Special Assistance Programme [Grant No. F.510/8/DRS/2004 (SAP-I)] sponsored by the University Grants Commission (UGC), New Delhi, India.

Appendix A

The expressions for $A_{i,j}, B_{i,j}, \ldots., H_{i,j}, S_{i,j}$ should be read, respectively, as

$$A_{i,j} = \frac{x_j R_i}{\delta z_i \partial zt} + \frac{x_j R_i}{\delta z_i \partial zb} + \frac{x_j^2 R_i \left(\frac{dR}{dz}\right)_{i+\frac{1}{2}} \delta z_{i+1} \delta x_{j+1}}{4R_{i+\frac{1}{2}} \delta x_j \delta z_i \partial zt \partial xt} - \frac{x_j^2 R_i \left(\frac{dR}{dz}\right)_{i+\frac{1}{2}} \delta z_{i+1} \delta x_{j-1}}{4R_{i+\frac{1}{2}} \delta x_j \delta z_i \partial zt \partial xb}$$
$$- \frac{x_j^2 R_i \left(\frac{dR}{dz}\right)_{i-\frac{1}{2}} \delta z_{i-1} \delta x_{j+1}}{4R_{i-\frac{1}{2}} \delta x_j \delta z_i \partial zb \partial xt} + \frac{x_j^2 R_i \left(\frac{dR}{dz}\right)_{i-\frac{1}{2}} \delta z_{i-1} \delta x_{j-1}}{4R_{i-\frac{1}{2}} \delta x_j \delta z_i \partial zb \partial xb} + \frac{x_{j+\frac{1}{2}}}{R_i \partial xt \delta x_j}$$
$$+ \frac{x_{j-\frac{1}{2}}}{R_i \partial xb \delta x_j},$$

$$B_{i,j} = -\frac{x_j R_i}{\delta z_i \partial zt} + \frac{x_j^2 R_i \left(\frac{dR}{dz}\right)_{i+\frac{1}{2}} \delta z_i \delta x_{j+1}}{4R_{i+\frac{1}{2}} \delta x_j \delta z_i \partial zt \partial xt} - \frac{x_j^2 R_i \left(\frac{dR}{dz}\right)_{i+\frac{1}{2}} \delta z_i \delta x_{j-1}}{4R_{i+\frac{1}{2}} \delta x_j \delta z_i \partial zt \partial xb},$$

$$C_{i,j} = -\frac{x_j R_i}{\delta z_i \partial zb} - \frac{x_j^2 R_i \left(\frac{dR}{dz}\right)_{i-\frac{1}{2}} \delta z_i \delta x_{j+1}}{4R_{i-\frac{1}{2}} \delta x_j \delta z_i \partial zb \partial xt} + \frac{x_j^2 R_i \left(\frac{dR}{dz}\right)_{i-\frac{1}{2}} \delta z_i \delta x_{j-1}}{4R_{i-\frac{1}{2}} \delta x_j \delta z_i \partial zb \partial xb},$$

$$D_{i,j} = \frac{x_j^2 R_i \left(\frac{dR}{dz}\right)_{i+\frac{1}{2}} \delta z_{i+1}}{4R_{i+\frac{1}{2}} \delta z_i \partial zt \partial xt} - \frac{x_j^2 R_i \left(\frac{dR}{dz}\right)_{i-\frac{1}{2}} \delta z_{i-1}}{4R_{i-\frac{1}{2}} \delta z_i \partial zb \partial xt} - \frac{x_{j+\frac{1}{2}}}{R_i \partial xt \delta x_j},$$

$$E_{i,j} = -\frac{x_j^2 R_i \left(\frac{dR}{dz}\right)_{i+\frac{1}{2}} \delta z_{i+1}}{4R_{i+\frac{1}{2}} \delta z_i \partial zt \partial xb} + \frac{x_j^2 R_i \left(\frac{dR}{dz}\right)_{i-\frac{1}{2}} \delta z_{i-1}}{4R_{i-\frac{1}{2}} \delta z_i \partial zb \partial xb} - \frac{x_{j-\frac{1}{2}}}{R_i \partial xb \delta x_j},$$

$$F_{i,j} = \frac{x_j^2 R_i \left(\frac{dR}{dz}\right)_{i+\frac{1}{2}}}{4R_{i+\frac{1}{2}} \partial zt \partial xt}, \quad G_{i,j} = -\frac{x_j^2 R_i \left(\frac{dR}{dz}\right)_{i+\frac{1}{2}}}{4R_{i+\frac{1}{2}} \partial zt \partial xb},$$

$$H_{i,j} = \frac{x_j^2 R_i \left(\frac{dR}{dz}\right)_{i-\frac{1}{2}}}{4R_{i-\frac{1}{2}} \partial zb \partial xb}, \quad \text{and} \quad S_{i,j} = -\frac{x_j^2 R_i \left(\frac{dR}{dz}\right)_{i-\frac{1}{2}}}{4R_{i-\frac{1}{2}} \partial zb \partial xt},$$

where $\partial zt = 0.5(\delta z_i + \delta z_{i+1}), \partial zb = 0.5(\delta z_i + \delta z_{i-1}), \partial xt = 0.5(\delta x_j + \delta x_{j+1})$ and $\partial xb = 0.5(\delta x_j + \delta x_{j-1})$.

References

[1] R. Ross, Atherosclerosis: a defense mechanism gone awry, Am. J. Pathol. 143 (1993) 987–1002.
[2] D.M. Wootton, D.N. Ku, Fluid mechanics of vascular systems, diseases and thrombosis, Annu. Rev. Biomed. Eng. 1 (1999) 299–329.
[3] S. Goldberg, P. Hahn, E. Halpern, R. Fogle, G.S. Gazelle, Radiofrequency tissue ablation: effect of pharmacological modulation of blood flow on coagulation diameter, Radiology 209 (1998) 761–767.
[4] S.B. Chinn, F.T. Lee Jr., G.D. Kennedy, C. Chinn, C.D. Johnson, T.C. Winter III, T.F. Warner, D.M. Mahvi, Effect of vascular occlusion on radiofrequency ablation of the liver: results in a porcine model, Amer. J. Roentgenology 176 (2001) 789–795.
[5] D.N. Ku, D.P. Giddens, C.K. Zarins, S. Glagov, Pulsatile flow and atherosclerosis in the human carotid bifurcation: positive correlation between plaque location and low and oscillating shear stress, Atherosclerosis 5 (1985) 293–302.
[6] M.H. Friedman, G.M. Hutchins, C.B. Bargeron, O.J. Deters, F.F. Mark, Correlation between intimal thickness and fluid shear in human arteries, Atherosclerosis 39 (1981) 425–436.
[7] M.R. Kaazempur-Mofrad, A.G. Isasi, H.F. Younis, R.C. Chan, D.P. Hinton, G. Sukhova, G.M. LaMuraglia, R.T. Lee, R.D. Kamm, Characterization of the atherosclerotic carotid bifurcation using MRI, finite element modeling, and histology, Ann. Biomed. Eng. 32 (2004) 932–946.
[8] A.K. Joshi, R.L. Leask, J.G. Myers, M. Ojha, J. Butany, C.R. Ethier, Intimal thickness is not associated with wall shear stress patterns in the human right coronary artery, Atheroscler. Thromb. Vasc. Biol. 24 (2004) 2408–2413.
[9] D.A. Steinman, J.B. Thomas, H.M. Ladak, J.S. Milner, B.K. Rutt, J.D. Spence, Reconstruction of carotid bifurcation hemodynamics and wall thickness using computational fluid dynamics and MRI, Magn. Reson. Med. 47 (2002) 149–159.
[10] C.G. Caro, J.M. Fitz-Gerald, R.C. Schroter, Atheroma and arterial wall shear. Observation, correlation and proposal of a shear dependent mass transfer mechanism for atherogenesis, Proc. R. Soc. Lond. B 177 (1971) 109–159.
[11] C.G. Caro, J.M. Fitz-gerald, R.C. Schroten, Proposal of a shear dependent mass transfer mechanism for atherogenesis, Clin. Sci. 40 (1971). 5 p..
[12] L.H. Back, J.R. Radbill, D.W. Crawford, Analysis of oxygen transport from pulsatile viscous blood flow to diseased coronary arteries of man, J. Biomech. 10 (1977) 763–774.
[13] P. Ma, X. Li, D.N. Ku, Heat and mass transfer in a separated flow region for high Prandtl and Schmidt numbers under pulsatile conditions, Int. J. Heat Mass Transfer 37 (1994) 2723–2736.
[14] G. Rappitsch, K. Perktold, Computer simulation of convective diffusion processes in large arteries, J. Biomech. 39 (1996) 207–215.
[15] S. Charm, B. Paltiel, G.S. Kurland, Heat transfer coefficients in blood flow, Biorheology 5 (1968) 133–145.
[16] S.A. Victor, V.L. Shah, Heat transfer to blood flowing in a tube, Biorheology 12 (1975) 361–368.
[17] S.A. Victor, V.L. Shah, Steady state heat transfer to blood flowing in the entrance region of a tube, Int. J. Heat Mass Transfer 19 (1976) 777–783.
[18] J.C. Chato, Heat transfer to blood vessels, J. Biomech. Eng. Trans. ASME 102 (1980) 110–118.
[19] J.J.W. Lagendijk, The influence of blood flow in large vessels on the temperature distribution in hyperthermia, Phys. Med. Biol. 27 (1982) 17–23.
[20] G.S. Barozzi, A. Dumas, Convective heat transfer coefficients in the circulation, J. Biomech. Eng. 113 (1991) 308–313.
[21] M.C. Kolios, M.D. Sherar, J.W. Hunt, Large blood vessel cooling in heated tissues: a numerical study, Phys. Med. Biol. 40 (1995) 477–494.
[22] S. Tungjitkusolmn, T. Staelin, D. Haemmerich, J.Z. Tsai, H. Cao, J.G. Webster, F.T. Lee Jr., D.M. Mahvi, V.R. Vorperian, Three dimensional finite element analysis for radio-frequency hepatic tumor ablation, IEEE Trans. Biomed. Eng. 49 (2002) 3–9.
[23] D. Haemmerich, A.S. Wright, D.M. Mahvi, F.T. Lee Jr., J.G. Webster, Hepatic bipolar radiofrequency ablation creates lesions close to blood vessels – a finite element study, Med. Biol. Eng. Comput. 41 (2003) 317–323.
[24] Y. Kawase, J.J. Ulbrecht, Heat and mass transfer in non-Newtonian fluid flow with power function velocity profiles, Can. J. Chem. Eng. 61 (1983) 791–800.
[25] I.C. Hung, Y. Perng, Flow of non-Newtonian fluid in the entrance region of a tube with porous walls, Int. J. Heat Fluid Flow 12 (1991) 263–268.
[26] R.S. Parikh, R. Mahalingam, Laminar tube flow heat transfer in non-Newtonian fluids under arbitrary wall heat flux, Int. Commun. Heat Mass Transfer 15 (1988) 1–16.

[27] M.E.S. Ahmed, H.A. Attia, Magnetohydrodynamic flow and heat transfer of non-Newtonian fluid in an eccentric annulus, Can. J. Phys. 76 (1998) 391–401.

[28] R.E. Nerem, Vascular fluid mechanics the arterial wall and arteriosclerosis, J. Biomech. Eng. Trans. ASME 114 (1992) 274–282.

[29] K.K. Yeleswarapu, Evaluation of continuum models for characterizing the constitutive behavior of blood, Ph.D. thesis, University of Pittsburgh, 1996.

[30] L.H. Back, Y.I. Cho, D.W. Crawford, R.F. Cuffel, Effect of mild atherosclerosis on flow resistance in a coronary artery casting of man, J. Biomech. Eng. Trans. ASME 106 (1984) 48–53.

[31] C.R. Ethier, Computational modeling of mass transfer and links to atherosclerosis, Ann. Biomed. Eng. 30 (2002) 461–471.

[32] A.A. Amsden, F.H. Harlow, The SMAC Method: A Numerical Technique for Calculating Incompressible Fluid Flow, Los Alamos Scientific Lab. Report LA-4370, 1970.

[33] J.E. Welch, F.H. Harlow, J.P. Shannon, B.J. Daly, The MAC Method, Los Alamos Scientific Lab. Report LA-3425, 1996.

[34] C.W. Hirt, Heuristic stability theory for finite difference equations, J. Comput. Phys. 2 (1968) 339–355.

[35] G. Markham, M.V. Proctor, C.E.G.B. Report TPRD/L/0063/M82, 1983.

[36] W.R. Milnor, Haemodynamics, Williams and Williams, Baltimore, 1992.

[37] A. Yakhot, L. Grinberga, N. Nikitin, Modeling rough stenoses by immersed-boundary method, J. Biomech. 38 (2005) 1115–1127.

[38] P.R. Johnston, D. Kilpatrick, Mathematical modelling of flow through an irregular arterial stenosis, J. Biomech. 24 (1991) 1069–1077.

[39] H.I. Andersson, R. Halden, T. Glomsaker, Effect of surface irregularities on flow resistance in differently shaped arterial stenoses, J. Biomech. 33 (2000) 1257–1262.

[40] O.I. Craciunescu, S.T. Clegg, Pulsatile blood flow effects on temperature distribution and heat transfer in rigid vessels, J. Biomech. Eng. Trans. ASME 123 (2001) 500–505.

[41] X. Deng, Y. Marois, M.W. King, R. Guidoin, Uptake of 3H-7-cholesterol along the arterial wall in an area of stenosis, ASAIO J. 40 (1994) 186–191.

[42] D.K. Stangeby, C.R. Ethier, Computational analysis of coupled blood-wall arterial LDL transport, J. Biomech. Eng. Trans. ASME 124 (2002) 1–8.